inorganics

MDPI

Article

Crystallographic Structure and Quantum-Chemical Analysis of Biologically Active Co(III)-Pyridoxal–Isothiosemicarbazone Complex

Fahad Abdulaziz [1], Khulood Fahad Alabbosh [2], Odeh Abdullah Odeh Alshammari [1], Wasan Mohammed Bin Tuwalah [1], Tahani Y. A. Alanazi [1], Aleksandra Rakić [3], Miljan Barić [3], Milica Marković [3], Violeta Jevtovic [1,*] and Dušan Dimić [3,*]

[1] Department of Chemistry, College of Science, University of Ha'il, Ha'il 81451, Saudi Arabia; odeh.alshammari@uoh.edu.sa (O.A.O.A.)
[2] Department of Biology, College of Science, University of Ha'il, Ha'il 81451, Saudi Arabia
[3] Faculty of Physical Chemistry, University of Belgrade, Studentski Trg 12-16, 11000 Beograd, Serbia; saska@ffh.bg.ac.rs (A.R.); milica.markovic@ffh.bg.ac.rs (M.M.)
* Correspondence: v.jevtovic@uoh.edu.sa (V.J.); ddimic@ffh.bg.ac.rs (D.D.)

Abstract: Semicarbazones and their transition metal complexes have been investigated as biologically active compounds. This study explores the synthesis, X-ray crystallographic structure, and characterization of a novel Co(III) complex cation with a pyridoxal-isothiosemicarbazone (PLITSC) ligand, $[Co(PLITSC\text{-}2H)(NH_3)_3]^+$. The structure of the complex was further elucidated by the elemental analysis and spectroscopic techniques (IR and UV–VIS). Hirshfeld surface analysis was applied for the investigation of intermolecular interactions governing crystal structure. Optimization was performed at the B3LYP/6-31 + G(d,p)(H,C,N,O,S)/LanL2DZ(Co) level of theory without any geometrical constraints. The selected level of theory's applicability was proven after comparing experimental and theoretical bond lengths and angles. The antibacterial activity of the complex towards *E. coli* and *B. subtilis* was determined and qualified as moderate compared to Streptomycin. The formation of free radical species in the presence of the complex was further verified in the fluorescence microscopy measurements. The molecular docking towards neural nitric-oxide synthase in the brain has shown that the complex structure and relative distribution of ligands were responsible for the binding to amino acids in the active pocket.

Keywords: DFT; Co complex; antimicrobial activity; methylene blue; QTAIM

Citation: Abdulaziz, F.; Alabbosh, K.F.; Alshammari, O.A.O.; Tuwalah, W.M.B.; Alanazi, T.Y.A.; Rakić, A.; Barić, M.; Marković, M.; Jevtovic, V.; Dimić, D. Crystallographic Structure and Quantum-Chemical Analysis of Biologically Active Co(III)-Pyridoxal–Isothiosemicarbazone Complex. *Inorganics* **2023**, *11*, 466. https://doi.org/10.3390/inorganics11120466

Academic Editors: Wolfgang Linert, Gabriel García Sánchez and Koichiro Takao

Received: 20 October 2023
Revised: 28 November 2023
Accepted: 29 November 2023
Published: 1 December 2023

1. Introduction

Today, there is considerable evidence that metal-based reagents are promising candidates for treating various diseases, particularly cancer. The discovery of cisplatin in the 1960s marked the beginning of the use of metal complexes in medicine [1]. Complexes based on transition metals are especially attractive due to their coordination geometry, which, using variations of ligands, enables the formation of numerous complexes with potential biological activity [2]. Despite the clinical success of cisplatin, many side effects are apparent, such as myelosuppression, nephrotoxicity, alopecia, and ototoxicity [3]. Therefore, there is a constant need for novel biologically active compounds with potential use as anticancer agents [4,5].

The synthesis of semicarbazone derivatives from pyridoxal and pyridoxal phosphate began with H. Cordes and P. Jencks in the early 1960s [6]. Later, in the 1980s, Italian chemists in Prof. Pelizzi's group introduced a group of ligands based on pyridoxal-carbazone [7,8]. From the beginning, these ligands seemed promising in terms of their ability to coordinate transition metal ions and their practical application as complexes with biological and catalytic activity [9].

Thus far, many papers in this field have been published describing the biological activities and catalytic abilities of numerous complexes with pyridoxal-semi-carbazone (PLSC) and pyridoxal-S-methyl-iso-thiosemi-carbazone (PLITSC) ligands. PLITSC is a tridentate ligand with the oxygen of phenolic hydroxyl, hydrazine nitrogen, and amino nitrogen as coordination sites through which the ONN form of the coordinated ligand is formed. It is formed by the synthesis of pyridoxal and S-methyl-isothiosemicarbazone (ITSC). The dehydration of ITSC with pyridoxal moiety (3-hydroxy-5-hydroxymethyl-2-methyl-pyridine-4-carbaldehyde) results in the formation of Schiff base ligands PLITSC (Scheme 1).

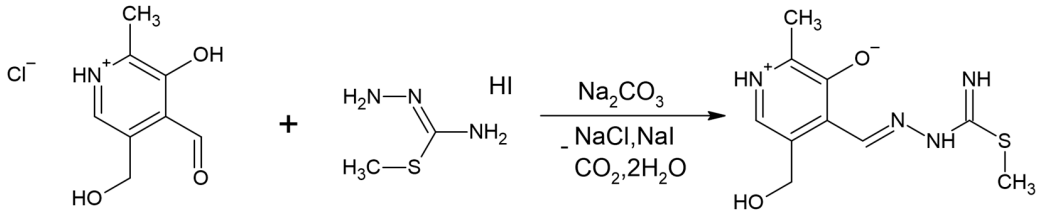

Scheme 1. Synthesis of pyridoxal–isothiosemicarbazone (PLITSC).

PLITSC can exist in three forms: neutral, monoanionic, and dianionic (Scheme 2). The monoanionic form is obtained by removing hydrogen from hydrazine nitrogen, while the doubly negative species is formed when pyridine nitrogen is deprotonated.

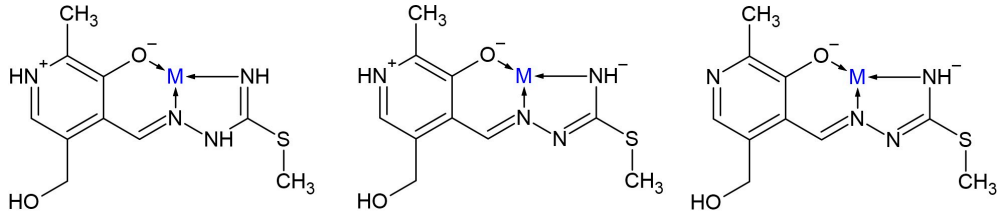

Scheme 2. Binding modes of differently protonated PLITSC (M is metal).

Complexes containing PLITSC and different transition metal ions have been described in the literature. The most numerous group includes copper compounds such as $(Cu(NO_3)(PLITSC)(H_2O)]NO_3$ [10]), $[Cu(PLITSC–2H)NH_3]H_2O \times 0.5MeOH$ [11], [Cu(ITSCPL–2H)$(NH_3)]_2 \times H_2O$ [12], $Cu(PLITSC)Br(CH_3OH)]Br$ [13], $Cu(PLITSC)Cl_2$, and Cu(PLITSC)Br_2 [14]. The complexes have shown promising antitumor, antiviral, and anti-inflammatory activities, in some cases higher than that of cisplatin [15]. Their potential use as materials for electrocatalytic hydrogen evolution has also been proven [16]. The second largest group of PLITSC-containing compounds has iron as a central metal ion, as in $Fe(PLITSC)Cl_3 \times H_2O$, $Fe(PLITSC)(PLITSC–H)](NO_3)_2 \times H_2O$, $[Fe(PLITSC)(PLITSC–H)]SO_4 \times 2H_2O$ [14], $Fe(PLITSC)Cl_3 \times H_2O$, $Fe(PLITSC)(PLITSC–H)](NO_3)_2 \times H_2O$, and $[Fe(PLITSC)(PLITSC–H)]SO_4 \times 2H_2O$ [9]. Cobalt, nickel, and other metal ions also easily coordinate with the mentioned ligand, some examples are $Co(PLITSC–2H)(PLITSC–H)] \times CH_3OH$ [17]; $[Co(PLITSC–H)_2]BrNO_3 \times CH_3OH$ [18], $Co(PLITSC)Cl_2] \times 2H_2O$, $[Co(PLITSC)(PLITSC–H)]Cl_2 \times 4H_2O$, $[Co(PLITSC–H)_2]Cl \times 2H_2O$, $[Co(PLITSC–H)(PLITSC–2H)]CH_3OH$, [Co(PLITSC)$(NH_3)_3]NO_3 \times 3H_2O$ [11], $[VO_2(PLITSC–H)] \times 2H_2O$, $[MoO_2(PLITSC–2H)]$ [19], and $[Ni(PLITSC)(H_2O)_3](NO_3)_2$ [20]. Over the past decade, the good catalytic properties of transition metal complexes with derivatives of pyridoxal-carbazone as ligands have been studied [16,21–25].

Cobalt is a transition metal of great biological relevance. It is an integral part of several cobalt-containing proteins, indirectly involved in DNA synthesis by acting as a B12 vitamin active center and vitamin supplement. All of this and the fact that it is less toxic than other non-essential metals led to the synthesis of many cobalt complexes with potential biological activity [26–31].

This study presents results on the synthesis and determination of the crystallographic structure of [Co(PLITSC–2H)$(NH_3)_3$]$(NO_3)_{0.491}Cl_{0.509}$) (**1**). The structural analysis also included elemental composition and IR and UV–VIS techniques. The theoretical methods based on Density Functional Theory were further employed to optimize structure. Antibacterial activity and reactive oxygen species formation were used to assess the biological activity of **1**. Molecular docking was used to analyze the possible interactions between compound **1** and proteins of interest.

2. Results

2.1. Crystallographic Structure

The synthesis of the Co(III) complex with PLITSC ligand is presented in Scheme 3. A 1:1 molar ratio of ligand and metal salt was used, and a mono-ligand complex was obtained. As already mentioned, the synthesis was conducted in an aqueous solution. The outer sphere comprises nitrate and chloride anions, and their molar fraction in the gross formula is particularly interesting. The complex [Co(PLITSC-2H)$(NH_3)_3$]$((NO_3)_{0.491}Cl_{0.509}$**)** is a compound with pseudo-octahedral geometry, and it includes an ONN ligand and three molecules of ammonia in coordination with Co(III) (Figure 1a). The coordinated PLITSC ligand is in the dianionic form, L^{2-}. The absence of hydrogen atoms on the pyridine and azomethine nitrogen (N9 and N5) is proof of the dianionic nature of the coordinated ligand. Anions (chloride and nitrate) are in the outer sphere. Considering the formula of the complex (one ligand in the dianionic form L^{2-}) and the level of participation of the anionic part of the outer sphere (Cl 0.509 and NO_3 0.491) (Figure 1), the charge on the cobalt ion is +3.

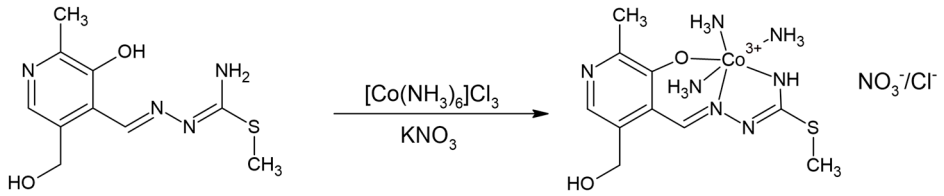

Scheme 3. Synthesis of [Co(PLITSC-2H)$(NH_3)_3$]$(NO_3)_{0.491}Cl_{0.509}$).

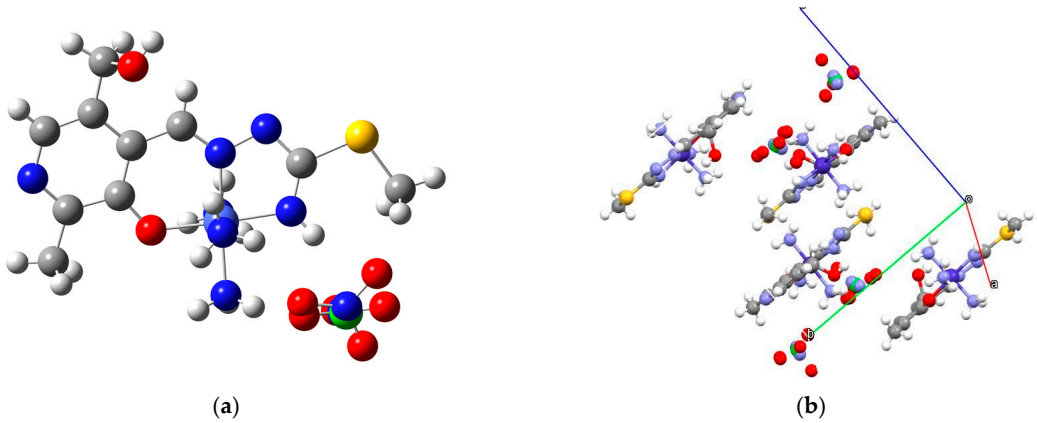

(**a**) (**b**)

Figure 1. (**a**) Crystal structure and (**b**) crystal package of [Co(PLITSC-2H)$(NH_3)_3$]$(NO_3)_{0.491}Cl_{0.509}$). (Hydrogen—white, carbon—gray, nitrogen—blue, oxygen—red, chlorine—green, cobalt—cyan).

A new structure of cobalt with pyridoxal-S-methylisothiosemicarbazone is similar to the structure already published in 2022 [18]. The structure [Co(PLITSC-H)$_2$]$BrNO_3 \cdot CH_3OH$ is a bis-ligand complex; two PLITSC ligands are in monoanionic form in the inner sphere. Anions, NO_3^- and Br^-, and ammonia ligands are absent because $CoCl_2$ dissolved in methanol was used for synthesis.

Tables S1 and S2 show bond lengths and angles around the central cobalt atom. Based on the angles, it can be concluded that it is an almost regular octahedron with minimal

deviations from the ideal (Figure 1). Four cobalt complex molecules are packed in a single cell, as shown in Figure 1b.

2.2. Spectral Analysis

The IR spectrum in the range between 4000 and 400 cm^{-1} of the obtained complex is shown in Figure S1. In the range between 2200 and 3700 cm^{-1}, there is a broad peak that includes specific X−H (X=C, N, O) stretching vibrations. The most intense peak at 3133 cm^{-1} is assigned to the O−H and N−H stretching vibrations [32,33]. Due to the multitude of ammonia ligands, this peak is very intense and shifts towards lower wavenumbers. The N−H stretching vibration of the ligand's amino group is also located in this area. These bands are shifted towards lower wavenumbers due to the formation of intermolecular hydrogen bonds within the crystal structure. It is important to observe that a complex network of interactions is formed, as presented in Figure 1b. The expected location of C−H stretching vibrations in the methyl groups is below 3000 cm^{-1}, while the C−H vibrations of aromatic hydrogen atoms are above 3000 cm^{-1}. These bands are probably covered by the other bands, mainly because their intensity is very low. The absence of the peak at 2850 cm^{-1}, characteristic of the neutral form of ligand, is additional proof that deprotonation of ligand occurred [34]. A strong peak at 1499 cm^{-1} is assigned to the C−N stretching vibrations [34]. The presence of oxygen atoms in the structure leads to two peaks depending on the bond's strength between carbon and oxygen atoms, presumably at 1167($(C-O)_{aliphatic}$) and 1237 cm^{-1} ($(C-O)_{aromatic}$). The rocking vibrations of ammonia ligands are located as a complex band with a peak at around 1255 cm^{-1}. The presence of nitrate anions is proven through the intense band at 1378 cm^{-1} [35].

A UV–VIS spectrum of **1** was recorded between 200 and 800 nm (Figure S2). It consists of two doublet-like structures at around 250 and 380, characteristic of pyridoxal and S-methyl-isothiosemicarbazone moieties. These maxima are assigned as $\pi \rightarrow \pi^*$ and $n \rightarrow \pi^*$ transitions for similar compounds [36]. Due to the complexation and charge transfer, these bands are very wide. The d-d bands were not present in spectra because of very low concentrations and the masking effect of other bands, as elaborated in references investigating similar complexes [37,38].

2.3. Hirshfeld Surface Analysis

The intermolecular interactions governing the crystal stability were assessed using the Hirshfeld surface analysis. It is beneficial to determine the contact atoms and percentages of different contacts since a multitude of species are found in the crystal structure. The Hirshfeld surface of the obtained complex is presented in Figure 2a, while fingerprint plots are shown in the Supplementary Materials (Figure S3).

Due to the presence of PLITSC and ammonia in the inner sphere and various anions in the outer sphere, the central metal ion is completely surrounded, and there are no interactions, including those involving Co(III). The most numerous interactions are denoted as H···H (48.1%), which is higher than the percentage obtained for [Co(PLITSC-H)$_2$]$BrNO_3 \cdot CH_3OH$ [18]. The hydrogen-containing ligands are responsible for these stabilization interactions. The nitrate ions and groups with oxygen are included in H···O contacts, with 23.1%. The other significant group of contacts is denoted as H···N (11.3%). These interactions are formed between pyridine-, amino-, hydrazine-, and ammonia-group nitrogen and hydrogen atoms. The number of interactions is similar to those previously described in the Co(III) complex, which proves that the interactions between complex cation units are greater than those with the surrounding anions. The red areas on the Hirshfeld surface represent close contacts, mainly hydrogen bonds. For example, the hydroxymethyl group is a hydrogen atom donor, while pyridine nitrogen is a hydrogen bond acceptor. Contacts between carbon and hydrogen atoms account for 5.5%, and weak hydrogen bonds between positively charged hydrogen atoms and π-electron clouds of aromatic parts are included in these percentages [39]. The sulfur atom is contained in the H···S (7.6) contacts. Other interactions that include oxygen atoms and C and N atoms

account for 1.1 and 0.6%. A similar trend was observed for the compounds containing other pyridoxal–semicarbazone ligands [40]. The contributions of the remaining contacts are negligible.

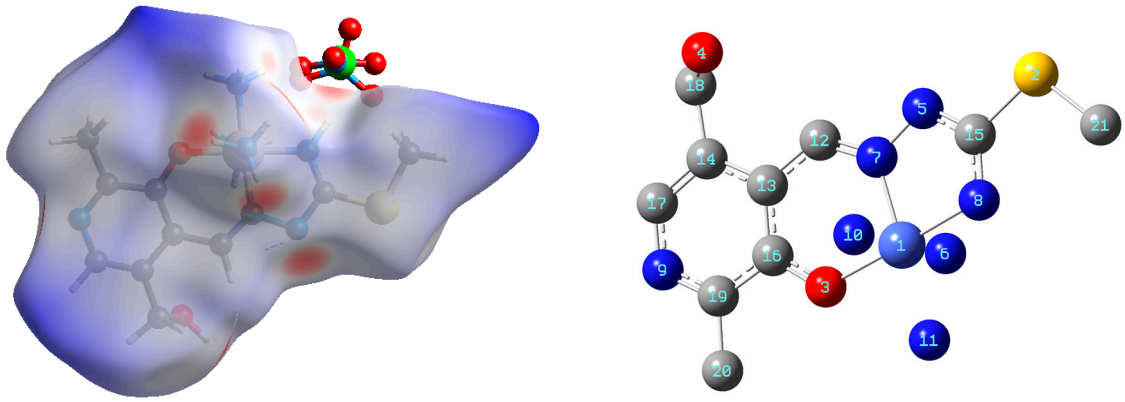

(**a**) (**b**)

Figure 2. (**a**) Hirshfeld surface and (**b**) optimized structure (at B3LYP/6-31 + G(d,p)(H,C,N,S,O)/LanL2DZ)(Co) of $[Co(PLITSC\text{-}2H)(NH_3)_3](NO_3)_2Cl$) (carbon—gray, oxygen-red, nitrogen—blue, cobalt—cyan; hydrogen atoms are omitted for clarity).

2.4. Theoretical Analysis, NBO and QTAIM Studies

The crystallographic structure of **1** was used for the optimization at the B3LYP/6-31 + G (d,p)(H,C,N,O,S)/LanL2DZ(Co) level of theory without any geometrical constraints. This theory level was previously applied to describe similar ligand systems regarding first-row transition metal complexes [18,40–42]. The applicability of this theoretical model was investigated by comparing the experimental and theoretical bond lengths and angles by calculating the correlation coefficient (R) and mean absolute error (MAE). The second parameter determines the average value of the difference between crystallographic and optimized structural parameters. Tables S1 and S2 present calculated values, while the optimized structure is shown in Figure 2b.

When the experimental and theoretical bond lengths and angles were compared, the following correlation coefficients were obtained: 0.99 and 0.98, respectively. The MAE value for bond lengths was 0.06 Å, while for bond angles, it was 1.6°. These differences are expected due to the relaxation of the system upon optimization [18]. The distance between phenolic oxygen and Co(III) is 1.89 Å in both structures. A difference of 0.05 Å was found for the bond distance between hydrazine nitrogen and central metal ions, which can be attributed to the partial relaxation of the system. The amino group of PLITSC forms an interaction with Co(III) with a distance of 1.89/1.93 Å in experimental/theoretical structure. Three ammonia ligands are distributed around central metal ions, with the two above the PLITSC plane being equal (N−Co bond length 1.993 Å in the optimized structure). This bond distance is elongated in the case of an ammonia molecule coplanar with PLITSC (2.05 Å). Due to the elongated delocalization of the electron cloud within the PLITSC structure, the bond lengths within the ligand are not significantly influenced by the complexation. Even before optimization, the crystallographic structure was almost a regular octahedron, which was limited because three donor atoms are part of the same ligand system. The angles O−Co−N_{hydr} and O−Co−N_{amino} are 96.1 and 82.1° in the optimized structure. On average, 1–2° were the discrepancies between experimental and theoretical bond angles, including amino groups. It is important to mention that the presence of ammonia ligands does not influence the bonding pattern between PLITSC and Co(III) when the structure of **1** is compared to literature data [18].

2.5. Antibacterial Activity

The emergence of bacterial resistance to antibiotics represents a significant global health concern [43–45]. There is a pressing necessity to explore novel, cost-effective therapeutic agents that have enhanced efficacy in addressing microbial illnesses and combating bacterial resistance. The antimicrobial effectiveness of compound **1** was assessed against two pathogenic bacterial species, *E. coli* and *B. subtilis*. The concentration ranges were adjusted from 0.25 to 2 mg mL^{-1}, and the zones of inhibition are presented in Table 1. The zone of inhibition increased in a concentration-dependent manner, between 8 and 23 mm for *E. coli* and 9 and 25 mm for *B. subtilis*. For the positive control, Streptomycin, the zone of inhibition was 14 mm for *E. coli* and 17 mm for *B. subtilis* when the lowest concentration was considered.

Table 1. Zone of inhibition of compound **1** and standard drug against tested bacteria.

Microorganisms	Concentration (mg mL^{-1})	Zone of Inhibition (mm)		
		Compound 1	Positive Control	Negative Control
E. coli	0.25	8 ± 0.2	14 ± 0.3	Zero inhibition
	0.5	13 ± 0.2		
	1	18 ± 0.2		
	2	23 ± 0.3		
B. subtilis	0.25	9 ± 0.2	17 ± 0.2	Zero inhibition
	0.5	14 ± 0.2		
	1	19 ± 0.3		
	2	25 ± 0.4		

The activity of this compound was found to be greater than those of other Co(III), Zn(II), Ni(II), and Cu(II) complexes with analogous ligands, as reported in previous research [18,40,46]. This study demonstrated that complexes comprising thiosemicarbazone and semicarbazone ligands have a moderately high activity against *E. coli* and *B. subtilis*. The observed difference in antibacterial activity can be ascribed to the disparity in the composition of the bacterial cell walls. *E. coli*, classified as a Gram-negative bacterium, possesses a relatively thin peptidoglycan layer and an outer lipopolysaccharide membrane (LPS) with a layered structure. In contrast, *B. subtilis*, classified as a Gram-positive bacterium, solely possesses a thick peptidoglycan layer without any other layers [47]. A cell wall in a bacterial cell facilitates the establishment of a distinct form and structure. Additionally, the cell wall serves a crucial function for bacteria by acting as a protective barrier against some particles and cells and as a potential target for certain antibiotics. Therefore, the findings of this study confirm that ROS were generated intracellularly due to the presence of the substances mentioned earlier. Furthermore, these ROS were found to be crucial in the suppression of detrimental activities exhibited by diverse microorganisms.

2.6. Minimum Inhibitory Concentration

The MIC of compound **1** was also evaluated against the mentioned microorganisms. Solutions with concentrations of compound **1** ranging from 20 to 60 μg mL^{-1} were prepared. Table 2 demonstrates that the MIC values for *E. coli* and *B. subtilis* were 40 and 30 μg mL^{-1}, respectively. On the other side, chloramphenicol was active towards both strains, even at the lowest concentration. These results also prove the moderate activity of **1** towards the investigated microorganisms. The observed outcomes are consistent with the findings of other experiments and can be ascribed to the generation of ROS. The results obtained in this study are comparable to analogous substances reported in the existing literature.

Table 2. Zone of inhibition of compounds **1** and **2** and standard drug against tested bacteria.

Compound	Bacterium	Concentration (μg mL^{-1})				
		60	50	40	30	20
Compound 1	*E. coli*	–	–	–	+	+
	B. subtilis	–	–	–	–	+
Chloramphenicol	*E. coli*	–	–	–	–	–
	B. subtilis	–	–	–	–	–

– represents strong inhibition of bacteria, + represents partial inhibition of bacteria.

2.7. ROS Generation

The formation of ROS within the bacterial cell was examined to understand a potential mechanism of antibacterial activity. Figure 3a,b illustrate the presence of intracellular ROS both before and after treatment with compound **1**. Figure 3a shows the absence of green fluorescence when irradiated with 488 nm in the case of untreated *E. coli*. The appearance of green fluorescence is evident in Figure 3b, where *E. coli* is represented as **1**. These results prove the assumption that ROS can be formed in the presence of compound **1**. These ROS include hydroxyl (OH·), superoxide anion radicals ($O_2 \cdot^-$), and hydrogen peroxide (H_2O_2). The 2,7-dichlorodihydrofluorescein diacetate undergoes oxidation in the presence of ROS, forming dichlorofluorescein. As a result, the ROS increased oxidative stress within the bacterial cells. The increasing oxidative stress leads to the elimination of intracellular species at the molecular level. The demise of bacteria occurs through the breakdown of macromolecules and cellular components, including the cell membrane, RNA, mitochondria, DNA, and different proteins within the cell [48,49].

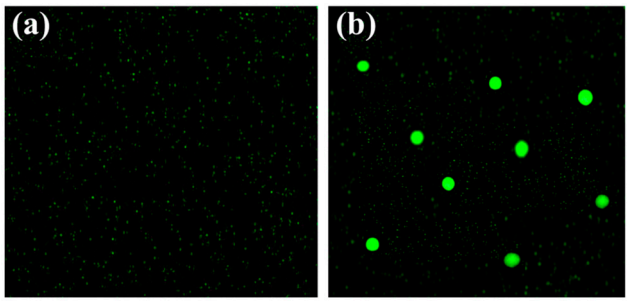

Figure 3. Determination of ROS in (**a**) absence and (**b**) presence of compound **1**.

2.8. Molecular Docking Studies

As no suitable target matches were found for the compounds, molecular docking studies involving proteins suggested by the Swiss Target Prediction web server as potential targets for the PLITSC molecule were performed. These proteins included matrix metalloproteinase 2 (PDB ID: 5I2Z [50]), cyclooxygenase-2 (PDB ID: 6BL4 [51]), protein farnesyltransferase (PDB ID: 2F0Y [52]), and neural nitric-oxide synthase in the brain (PDB ID: 4UH6 [53]). The docking calculations were performed on refined protein crystal structures extracted from the Protein Data Bank (PDB) with water and small molecules removed. The most promising results were obtained with the neural nitric-oxide synthase (brain nNOS or NOS-1), where all ligands exhibited successful binding within the active sites of the nNOS enzyme.

nNOS, or Nitric Oxide Synthase 1, is a pivotal signaling protein within the nervous system. It operates in an active state as a homodimer, with the transfer of electrical signals occurring from one dimer to another monomer. The monomeric structure of neuronal NOS (nNOS) reveals a bidomain architecture comprising an oxygenase domain located at the N-terminal and a reductase domain positioned at the C-terminal, separated by a calmodulin-binding motif. The oxygenase domain, responsible for binding the substrate L-arginine, encompasses essential functional sites, including a tetrahydrobiopterin (BH4)

binding site and a cytochrome P-450-type heme active site. Furthermore, a dedicated binding site for zinc (Zn) plays a crucial role in facilitating the dimerization of nNOS. Neuronal NOS's multifaceted functions encompass its involvement in synaptic plasticity within the central nervous system (CNS), which contributes to the relaxation of smooth muscles, regulates central blood pressure, and promotes vasodilation through peripheral nerves [54,55].

All ligands exhibit the capacity to bind within the active sites of the nNOS enzyme. However, their binding energies are notably lower compared to naturally bound ligands. In molecular docking simulations on the nNOS dimer, complex **1** binds to distinct active sites within the nNOS molecule. Specifically, this compound binds proximate to the hemoglobin (HEM) molecule binding site in chains A and B, as shown in Figure 4. The binding energies for **1** are notably lower in both nNOS monomers, registering at -32.2 and -28.5 kJ mol^{-1}, as opposed to the HEM molecule with significantly higher binding energies of -43.1 and -42.2 kJ mol^{-1}. Notably, these active sites are not the primary choice for binding HEM; they rank fifth in preference.

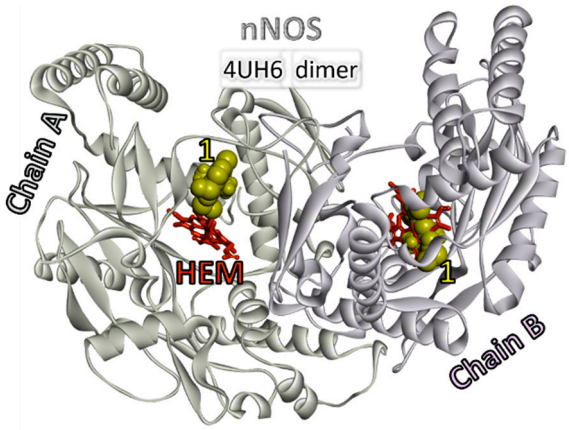

Figure 4. Depiction of the nNOS dimer (PDB ID: 4UH6) composed of two monomers, Chain A and Chain B. Hemoglobin (HEM), functioning as a prosthetic group, is presented as a light brown structure, occupying the heme binding pockets within both chains. The computationally docked complex is rendered in CPK style, visualized as spherical balls, and color coded in yellow.

The preferred binding location for **1** in chain A is the space above the active site for HEM, where it interacts with amino acids Arg704, Phe709, Glu710, Ser416, and Ser418 (Figure 5). Most of these interactions involve classical hydrogen bonds established via ammonia molecules within the structure of **1**. Additionally, there are cation–π interactions and some hydrophobic interactions. In chain B, the obtained complex binds to the HEM active site and interacts with Cys420, Val572, Phe589, Trp592, and Glu592. Only one ammonia molecule is involved in establishing three hydrogen bonds. Furthermore, π-sulfur and $\pi-\pi$ T$-$shaped interactions are observed.

Interestingly, the PLITSC ligand appears to dictate the binding positions within the nNOS molecule, occupying the same sites as the complexes mentioned earlier. However, the presence of other ligands in complexes with cobalt (ammonia molecules) intensifies and increases the number of favorable interactions. The binding energies are the lowest for PLITSC, amounting to -29.3 kJ mol^{-1} in chain A and even lower at -28.0 kJ mol^{-1} in chain B. The PLITSC molecule interacts with amino acids Thr329, Ser418, Arg419, Asn702, Glu710, Cys331, and Cys336, with hydrogen bonds being the primary mode of interaction. Hydrophobic interactions are also evident. In isolated PLITSC molecules, the formation of the complex formation occurs, but interactions with the π system of the aromatic ring are not observed. Nonetheless, interactions involving amino groups, nitrogen, and oxygen atoms are prominent. In chain B, interactions are limited, established only with amino acids Arg419, Cys420, and Asp680, including hydrophobic interactions, classic hydrogen

bonds, and carbon–hydrogen bonds. The bound PLITSC molecule coincides with the HEM active site.

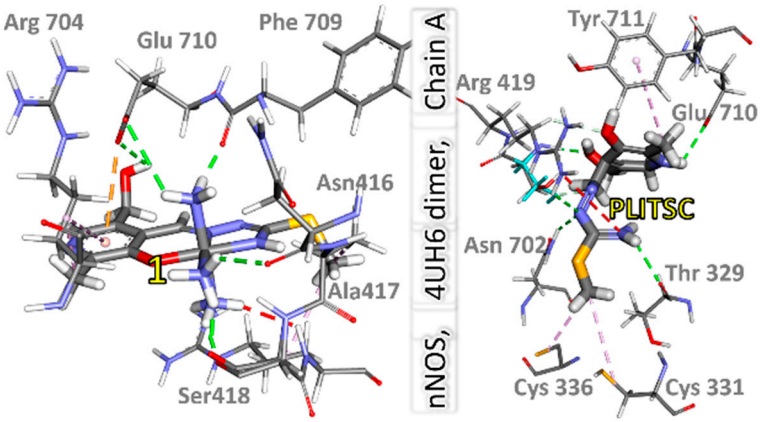

Figure 5. Visualization of intermolecular interactions of the complex (1) and PLITSC above the heme binding site of chain A in the nNOS molecule (PDB ID: 4UH6).

3. Materials and Methods

3.1. Chemicals and Instruments

All commercially obtained reagent-grade chemicals were used without further purification. The ligand, pyridoxal-isothio-semicarbazone, was prepared according to the described procedures [14]. The elemental analyses (C, H, N, and S) of air-dried samples were conducted on an Elementar Vario El III (Elementar Analysensysteme GmbH, Langenselbold, Germany). The measurements were repeated three times and analyzed through oxidation at 1200 °C. The gaseous oxides were then separated in a column using a carrier gas (helium). The mass percentages were calculated based on the intensity corresponding to different oxides. The infrared spectra were recorded on a Thermo Nicolet-Avatar 370 FTIR spectrometer (Thermo Fisher Scientific, Waltham, MA, USA) between 4000 and 400 cm^{-1}. The KBr pellet technique was used with the 1:KBr = 3 mg:150 mg mass ratio. The UV–VIS spectrum between 200 and 800 nm was obtained on a Thermo Scientific UV–VIS Spectrophotometer (Thermo Fisher Scientific, Waltham, MA, USA) with a resolution of 1 nm and integration time of 0.20 s.

3.2. Synthesis of [Co(PLITSC-2H)(NH_3)$_3$]($(NO_3)_{0.491}Cl_{0.509}$) Crystal

In 15 cm^3 of water 0.01 mol of PLITSC ligand was heated and dissolved. An aqueous solution of 0.01 mol of $[Co(NH_3)_6]Cl_3$ and 0.005 mol of KNO_3 in 15 cm^3 was also prepared and added to the ligand solution, as presented below. KNO_3 was included to increase the solubility of the complex cobalt(III) salt, and nitrate ions were necessary for the competitive binding with cobalt(III). A clear purple solution was obtained and left at room temperature to crystallize using the slow evaporation method. After a few hours, purple crystals appear. Yield: 0.16 g (65%). Anal. Calcd for $C_{10}H_{21}CoN_7O_2S$, 0.509(Cl) 0.491(NO_3) (410.83): C, 29.21; H, 5.11; N, 25.28; S, 7.79. Found: C, 29,19; H, 5.118; N, 25.33; S, 7.70. IR: υ (cm^{-1}) 3133 (s), 2850 (s), 1499 (m), 1378 (s), 1307 (m), 1255 (w), 1237 (w), 1167 (s), 1036 (w), 903 (w), 746 (w). UV–VIS: 218, 250, 344, 413 nm.

3.3. X-ray Analysis

A single crystal of size 0.12 × 0.09 × 0.17 mm was obtained and submitted for the X-ray diffraction analysis. This crystal was mounted on a glass fiber and examined at 296 K on a Bruker D8 Venture APEX diffractometer (Bruker, Billerica, MA, USA) equipped with a Photon 100 CCD area detector using graphite–monochromate Mo-Kα radiation [λ = 0.71073 Å]. The absorption corrections were carried out with the SCALE3 ABSPACK algorithm implemented in the CrysAlisPro software (Rigaku, Cedar Park, TC, USA) [56]. Direct methods were used for solving the structure with SHELXS-2013. Positions of

non-hydrogen atoms (including chlorine and nitrate ions) were refined with anisotropic parameters using weighted full-matrix least squares on F^2. The presence of chlorine and nitrate ion constitutes substitutional disorder. PART instruction within SHELXL program was used to find the position and population for each atom within the anion structures. Restraints on nitrogen–oxygen bond length were applied. On the other hand, hydrogen atoms bonded to carbon atoms were placed in the calculated positions, according to the riding model. The positions of oxygen- and nitrogen-bonded hydrogen atoms were obtained from different Fourier maps and refined with appropriate constraints. Hydrogen positions were checked for feasibility by examining the hydrogen-bonding network. Crystallographic data were deposited in the Cambridge Crystallographic Data Centre (CCDC, 12 Union Road, Cambridge CB2 IEZ, UK; e-mail: depos-it@ccdc.cam.ac.uk), CCDC number 2277681. Crystal data collection and structure refinement are provided in Table 3.

Table 3. Crystal data and structure refinement details of compound **1**.

Empirical Formula	**$C_{10}H_{21}CoN_7O_2S$, 0.509(Cl) 0.491(NO_3)**
Formula weight [g mol^{-1}]	410.83
Temperature [K]	123 K
Wavelength [Å]	1.54184
Crystal system	monoclinic
Space group	$P2_1/n$
Volume [$Å^3$]	2018.70(6)
Unit cell dimension [Å, deg]	a = 11.1588(7) b = 12.5163(5) c = 15.1557(2) α = 90 β = 107.505(1) γ = 90
Z	4

3.4. Hirshfeld Surface Analysis

The intermolecular interactions that are important for the stability of crystal structure were investigated using the Hirshfeld surface analysis. CrystalExplorer program [57] was employed to analyze contacts between atoms within the crystallographic structure. This surface analysis is presented in a graph connecting two distances, one between the two nearest nuclei (de) and the other between the nuclei and external surface (di) [41,58,59]. The distances are normalized and colored depending on the van der Waals radii separation. Red, white, and blue colors are applied if the separation is shorter, equal, or longer than these radii. The normalized distances are between −0.9901 (red) and 2.8692 (blue). Fingerprint plots present the specific contact points between atoms and the relative percentages of these contacts in the total number of interactions. Fingerprint plots are shown in the Supplementary Materials.

3.5. Theoretical Analysis

The crystallographic structure was optimized in the Gaussian 09 [60] Program Package (Gaussian 09, Revision C 01) without any geometrical constraints. The following levels of theory were applied: B3LYP/6-31 + G(d,p) non-metallic atoms (H, C, N, O, S) [61,62] and B3LYP/LanL2DZ for Co [63,64]. This level of theory was previously applied for the transition metal complexes containing similar ligand systems [18,40–42] and allowed the assignation of the spectra and reactivity assessment. The minimum on the potential energy surface was obtained, as shown by the absence of imaginary frequencies. Several spin states were optimized, and the one that resembled the crystallographic structure the most was later used throughout the paper.

3.6. Antibacterial Activity

The agar well diffusion method is widely recognized for assessing compounds' antibacterial efficacy [65–67]. The procedure entails cultivating bacterial cells, *Escherichia coli*, and *Bacillus subtilis*, in an LB (Luria–Bertani) medium for approximately 24 h in the incubator set at 37 °C. Aseptic swabs were utilized to streak the inoculum of the mentioned bacterium onto the Muller–Hinton agar plate. A sterilized cork borer was employed to create wells measuring 6 mm in diameter on the nutrient agar (Merck, Darmstadt, Germany) plates. Subsequently, a 50 µL aqueous solution containing different concentrations of compound **1** (0.25, 0.5, 1, and 2 mg mL^{-1}) was inserted into the wells. The nutritional agar dishes were carefully shifted to an incubator set at 37 °C, where they were allowed to incubate for 24 h. In this study, Streptomycin was employed as the standard.

3.7. Reactive Oxygen Species (ROS) Generation

The production of ROS was facilitated through the utilization of 2,7-dichlorodihydrofluorescein diacetate (DCFH-DA) [68]. This dye is highly effective for evaluating the reactive oxygen species (ROS) levels in bacterial cells due to the oxidative stress caused by external substances. The *E. coli* bacterial strain was incubated for approximately three hours with a specified amount of compound **1**. The *E. coli* cell culture was centrifuged at 1000 rpm for 15 min and washed with phosphate-buffered saline (PBS) solution. Subsequently, 1 mL of solution containing 20 mM of 2,7-dichlorofluorescein diacetate was mixed with the suspension for 60 min. Finally, the cells were subjected to an ethanol rinse to remove the excess dye. Excitation and emission fluorescence were followed by a fluorescence microscope, with an excitation wavelength set to 488 nm and emission recorded at 535 nm [69,70].

3.8. Minimum Inhibition Concentration (MIC)

A serial dilution technique was applied to determine the minimum inhibitory concentration (MIC) of compound **1** against the selected microorganisms [71,72]. Solutions of various concentrations (ranging from 20 to 120 µg mL^{-1}) of compound **1** were prepared. A volume of 1 mL was taken from each standard solution and transferred into a sterile test tube. This portion was combined with 1 mL of a bacterial solution, including *E. coli* and *B. subtilis,* with a turbidity standard of 0.5 McFarland. The tubes were placed in a shaking incubator for 24 h at 37 °C. The MIC was determined by employing the Beckman DU-70 UV–VIS Spectrophotometer (Beckman Coulter, Brea, CA, USA) utilizing the minimal concentration tube that exhibited the highest level of reduction in bacterial growth. The test tube without compound 1 was considered as a negative control. All measurements were repeated three times.

3.9. Molecular Docking Analysis

The optimized structure of **1** was used for the protein binding studies. The PLITSC ligand was extracted from the original Co-complex and independently optimized at the B3LYP/6-31 + G(d,p) level of theory. The Swiss Target Prediction web server [73,74] was employed to identify potential target proteins for these compounds. Notably, only a few matches were found for PLITSC, while this platform failed to locate suitable targets for complexes. Molecular docking calculations were performed on all suggested targets for the PLITSC ligand to determine the most relevant target protein. Small molecules and target proteins were prepared for docking calculations using AutoDockTools4 [75] software. The actual docking calculations were executed employing AutoDockVina [76] software. Finally, BIOVIA Discovery Studio [77] was employed for the visualization and in-depth data analysis of the docking results.

4. Conclusions

A novel Co(III) with pyridoxal–isothiosemicarbazone (PLITSC) was synthesized and characterized using an elemental analysis, IR and UV–VIS spectroscopies, and X-ray crystallography. PLITSC is in a dianionic form and, together with three ammonium molecules, forms

an octahedral geometry around a central metal ion. In the outer sphere, nitrate and chloride anions are present. The highest number of interactions are formed between hydrogen atoms and electronegative elements, as shown in the Hirshfeld surface analysis. The crystallographic structure was optimized at the B3LYP/6-31 + G(d,p)(H,C,N,O,S)/LanL2DZ(Co) level of theory. High correlation coefficients (>0.98) and low MAE values proved the applicability of the chosen level of theory. Compared to Streptomycin, the title compound was moderately active toward *E. coli* and *B. subtilis*. The minimum inhibitory concentrations of the complex against *E. coli* and *B. subtilis* were 40 and 30 μg mL^{-1}, respectively. The underlying mechanism of antibacterial activity could be the production of the reactive oxygen species, as shown in the experiment with 2,7-dichlorodihydrofluorescein. Complex **1** interacted with the amino acids of the active pocket of Nitric Oxide Synthase 1 in the same position as hemoglobin. The most important interactions originated from the PLITSC ligand, which showed that this ligand dictated the binding position. The strength of interactions between other ligands was negligible. These promising results should be further examined for the possible applications of the obtained complex.

Supplementary Materials: The following supporting information can be downloaded at: https://www.mdpi.com/article/10.3390/inorganics11120466/s1, Table S1: Crystallographic and optimized (at B3LYP/6-31 + G(H,C,N,S,O)/LanL2DZ(Co)) bond lengths (in Å) of $[Co(PLITSC\text{-}2H)(NH_3)_3]^+$; Table S2: Crystallographic and optimized (at B3LYP/6-31 + G(H,C,N,S,O)/LanL2DZ(Co)) bond angles (in °) of $[Co(PLITSC\text{-}2H)(NH_3)_3]^+$; Figure S1: IR spectrum of 1; Figure S2: UV–VIS spectrum of 1; Figure S3: The fingerprint plots for the most important interactions within crystal structure of **1**.

Author Contributions: Conceptualization, F.A., A.R., V.J. and D.D.; methodology, K.F.A., O.A.O.A., W.M.B.T. and T.Y.A.A.; software, M.B., M.M. and A.R.; validation, M.B. and F.A.; formal analysis, K.F.A., O.A.O.A., W.M.B.T. and T.Y.A.A.; investigation, M.M. and M.B.; resources, V.J.; data curation, F.A., K.F.A., O.A.O.A., W.M.B.T. and T.Y.A.A.; writing—original draft preparation, A.R., M.M. and M.B.; writing—review and editing, D.D., F.A., K.F.A., O.A.O.A. and W.M.B.T.; visualization, D.D., A.R., M.B. and M.M.; supervision, D.D.; project administration, V.J. and T.Y.A.A.; funding acquisition, V.J. All authors have read and agreed to the published version of the manuscript.

Funding: This research was funded by Scientific Research Deanship at University of Ha'il, Kingdom of Saudi Arabia, through Project number RG-22015.

Data Availability Statement: Data are contained within this article.

Acknowledgments: The authors are thankful to the University of Ha'il, Kingdom of Saudi Arabia, for budgetary assistance from the Scientific Research Deanship (project number RG-22015).

Conflicts of Interest: The authors declare no conflict of interest. The funders had no role in the design of the study; in the collection, analyses, or interpretation of data; in the writing of the manuscript; or in the decision to publish the results.

References

1. Kenny, R.G.; Marmion, C.J. Toward Multi-Targeted Platinum and Ruthenium Drugs—A New Paradigm in Cancer Drug Treatment Regimens? *Chem. Rev.* **2019**, *119*, 1058–1137. [CrossRef] [PubMed]
2. Karges, J.; Stokes, R.W.; Cohen, S.M. Metal complexes for therapeutic applications. *Trends Chem.* **2021**, *3*, 523–534. [CrossRef] [PubMed]
3. Johnstone, T.C.; Suntharalingam, K.; Lippard, S.J. The Next Generation of Platinum Drugs: Targeted Pt(II) Agents, Nanoparticle Delivery, and Pt(IV) Prodrugs. *Chem. Rev.* **2016**, *116*, 3436–3486. [CrossRef] [PubMed]
4. Conti, L.; Macedi, E.; Giorgi, C.; Valtancoli, B.; Fusi, V. Combination of light and Ru(II) polypyridyl complexes: Recent advances in the development of new anticancer drugs. *Coord. Chem. Rev.* **2022**, *469*, 214656. [CrossRef]
5. Clarke, M.J. Ruthenium metallopharmaceuticals. *Coord. Chem. Rev.* **2002**, *232*, 69–93. [CrossRef]
6. Cordes, E.H.; Jencks, W.P. Semicarbazone Formation from Pyridoxal, Pyridoxal Phosphate, and Their Schiff Bases. *Biochemistry* **1962**, *1*, 773–778. [CrossRef] [PubMed]
7. Ferrari, M.B.; Fava, G.G.; Pelizzi, C.; Tarasconi, P.; Tosi, G. Thiosernicarbazones as Co-ordinating Agents. Part 2.* Synthesis, Spectroscopic Characterization, and X-Ray Structure of Aquachloro(pyridoxal thiosemicarbazone) manganese(II) Chloride and Aqua(pyridoxal thiosernicarbazonato)- copper(II) Chloride Monohydra. *J. Chem. Soc. Dalt. Trans.* **1987**, 227–233. [CrossRef]
8. Ferrari, M.B.; Fava, G.G.; Tarasconi, P. Thiosemicarbazones as Co-ordinating Agents. Part 3. Synthesis, Spectroscopic Characterization, and X-Ray Structure of Methyl Pyruvate Thiosemicarbazone Hemihydrate, Chloro(ethy1 pyruvate thiosemicar-

bazonato)copper(II) (Green Form), and Chloro (pyruvic acid thiosemicarbazonato) copper (II) dihydrate (blue form). *J. Chem. Soc. Dalt. Trans.* **1989**, 361–366. [CrossRef]
9. Mir, I.A.; Ain, Q.U.; Qadir, T.; Malik, A.Q.; Jan, S.; Shahverdi, S.; Nabi, S.A. A review of semicarbazone-derived metal complexes for application in biomedicine and related fields. *J. Mol. Struct.* **2024**, *1295*, 136216. [CrossRef]
10. Leovac, V.M.; Jevtović, V.S.; Bogdanovic, G.A. Transition metal complexes with thio-semicarbazide-based ligands. XLIV1. Aqua(3-hydroxy-5-hydroxymethyl-2-methylpyridine-4- carboxaldehyde 3-methylisothiosemicarbazone-κ3O, N1, N4)nitratocopper(II) nitrate. *Acta Crystallogr. Sect. C Cryst. Struct. Commun.* **2002**, *58*, m514–m516. [CrossRef]
11. Leovac, V.M.; Jevtović, V.S.; Jovanović, L.S.; Bogdanović, G.A. Metal complexes with schiff-base ligands-pyridoxal and semicarbazide-based derivatives. *J. Serbian Chem. Soc.* **2005**, *70*, 393–422. [CrossRef]
12. Jevtovic, V. Synthesis, Characterization and X-ray Crystal Structure of the Dimer Complex [Cu(PLITSC-2H)$(NH_3)]_2 \cdot 2H_2O$. *Am. J. Chem.* **2013**, *3*, 148–152.
13. Jevtovic, V. Synthesis and Structural Analysis of a Cu(II) Complex Incorporating Pyridoxal-S-Methylisothiosemicarbazone (PLITSC) Ligand. *Am. J. Chem.* **2014**, *4*, 47–50.
14. Jevtovic, V. *Cu, Fe, Ni and V Complexes with Pyridoxal Semicarbazones, Synthesis, Physical and Chemical Properties, Structural Analyses and Biological Activities*; Lambert Academic Publishing: London, UK, 2010.
15. Singh, N.K.; Kumbhar, A.A.; Pokharel, Y.R.; Yadav, P.N. Anticancer potency of copper(II) complexes of thiosemicarbazones. *J. Inorg. Biochem.* **2020**, *210*, 111134. [CrossRef] [PubMed]
16. Al-Zahrani, S.; Jevtovic, V.; Alenezi, K.; El, M.; Haque, A.; Vidovic, D. Electrocatalytic hydrogen evolution upon reduction of pyridoxal semicarbazone and thiosemicarbazone-based Cu(II) complexes. *J. Serbian Chem. Soc.* **2022**, *87*, 345–354. [CrossRef]
17. Jevtovic, V.; Cvetkovic, D.; Vidovic, D. Synthesis, X-ray characterization and antimicrobial activity of iron(II) andcobalt(III) complexes with the schiff base derived from pyridoxal and semicarbazide or S-methylisothiosemicarbazide. *J. Iran. Chem. Soc.* **2011**, *8*, 727–733. [CrossRef]
18. Jevtović, V.; Hamoud, H.; Al-zahrani, S.; Alenezi, K.; Latif, S.; Alanazi, T.; Abdulaziz, F.; Dimić, D. Synthesis, Crystal Structure, Quantum Chemical Analysis, Electrochemical Behavior, and Antibacterial and Photocatalytic Activity of Co Complex with pyridoxal-(S-methyl)-isothiosemicarbazone ligand. *Molecules* **2022**, *27*, 4809. [CrossRef] [PubMed]
19. Leovac, V.M.; Divjaković, V.; Joksović, M.D.; Jovanović, L.S.; Vojinović-Ješić, L.S.; Češljević, V.I.; Mlinar, M. Transition metal complexes with thiosemicarbazide-based ligands. Part 57. Synthesis, spectral and structural characterization of dioxovanadium(V) and dioxomolybdenum(VI) complexes with pyridoxal S-methylisothiosemicarbazone. *J. Serbian Chem. Soc.* **2010**, *75*, 1063–1074. [CrossRef]
20. Jevtovic, V.; Vidovic, D. Synthesis, characterization and X-Ray crystal structure of the tri aqua (3-Hydroxy-5-Hydroxymethyl-2-Methylpyridine- 4-Carboxaldehyde-3- Methylisotiosemicarbazone: k3, O3, N7, N 10) Ni(II) nitrate. *J. Chem. Crystallogr.* **2010**, *40*, 794–798. [CrossRef]
21. Manikandan, R.; Anitha, P.; Prakash, G.; Vijayan, P.; Viswanathamurthi, P. Synthesis, spectral characterization and crystal structure of Ni(II) pyridoxal thiosemicarbazone complexes and their recyclable catalytic application in the nitroaldol (Henry) reaction in ionic liquid media. *Polyhedron* **2014**, *81*, 619–627. [CrossRef]
22. Manikandan, R.; Anitha, P.; Viswanathamurthi, P.; Malecki, J.G. Palladium(II) pyridoxal thiosemicarbazone complexes as efficient and recyclable catalyst for the synthesis of propargylamines by a three-component coupling reactions in ionic liquids. *Polyhedron* **2016**, *119*, 300–306. [CrossRef]
23. Manikandan, R.; Anitha, P.; Prakash, G.; Vijayan, P.; Viswanathamurthi, P.; Butcher, R.J.; Malecki, J.G. Ruthenium(II) carbonyl complexes containing pyridoxal thiosemicarbazone and trans-bis(triphenylphosphine/arsine): Synthesis, structure and their recyclable catalysis of nitriles to amides and synthesis of imidazolines. *J. Mol. Catal. A Chem.* **2015**, *398*, 312–324. [CrossRef]
24. Pisk, J.; Prugovečki, B.; Matković-Čalogović, D.; Poli, R.; Agustin, D.; Vrdoljak, V. Charged dioxomolybdenum(VI) complexes with pyridoxal thiosemicarbazone ligands as molybdenum(V) precursors in oxygen atom transfer process and epoxidation (pre)catalysts. *Polyhedron* **2012**, *33*, 441–449. [CrossRef]
25. Jevtovic, V.; Alenezi, K.M.; El Moll, H.; Haque, A.; Al-Zahrani, S.A.; Humaidi, J.; Vidovic, D. Hydrogen Evolution Reaction Performance of Co(II) and Co(III) Complexes Based on pyridoxal (thio)semicarbazones. *J. Chem. Soc. Pakistan* **2021**, *43*, 673–681. [CrossRef]
26. Saranya, J.; Jone Kirubavathy, S.; Chitra, S.; Zarrouk, A.; Kalpana, K.; Lavanya, K.; Ravikiran, B. Tetradentate Schiff Base Complexes of Transition Metals for Antimicrobial Activity. *Arab. J. Sci. Eng.* **2020**, *45*, 4683–4695. [CrossRef]
27. Basha, M.T.; Alghanmi, R.M.; Shehata, M.R.; Abdel-Rahman, L.H. Synthesis, structural characterization, DFT calculations, biological investigation, molecular docking and DNA binding of Co(II), Ni(II) and Cu(II) nanosized Schiff base complexes bearing pyrimidine moiety. *J. Mol. Struct.* **2019**, *1183*, 298–312. [CrossRef]
28. Ganji, N.; Chityala, V.K.; Marri, P.K.; Aveli, R.; Narendrula, V.; Daravath, S. Shivaraj DNA incision evaluation, binding investigation and biocidal screening of Cu(II), Ni(II) and Co(II) complexes with isoxazole Schiff bases. *J. Photochem. Photobiol. B Biol.* **2017**, *175*, 132–140. [CrossRef]

29. Icsel, C.; Yilmaz, V.T.; Aydinlik, Ş.; Aygun, M. New manganese(II), iron(II), cobalt(II), nickel(II) and copper(II) saccharinate complexes of 2,6-bis(2-benzimidazolyl)pyridine as potential anticancer agents. *Eur. J. Med. Chem.* **2020**, *202*, 112535. [CrossRef]
30. Munteanu, C.R.; Suntharalingam, K. Advances in cobalt complexes as anticancer agents. *Dalt. Trans.* **2015**, *44*, 13796–13808. [CrossRef]
31. Beebe, S.J.; Celestine, M.J.; Bullock, J.L.; Sandhaus, S.; Arca, J.F.; Cropek, D.M.; Ludvig, T.A.; Foster, S.R.; Clark, J.S.; Beckford, F.A.; et al. Synthesis, characterization, DNA binding, topoisomerase inhibition, and apoptosis induction studies of a novel cobalt(III) complex with a thiosemicarbazone ligand. *J. Inorg. Biochem.* **2020**, *203*, 110907. [CrossRef]
32. Osman, U.M.; Silvarajoo, S.; Kamarudin, K.H.; Tahir, M.I.M.; Kwong, H.C. Ni(II) complex containing a thiosemicarbazone ligand: Synthesis, spectroscopy, single-crystal X-ray crystallographic and conductivity studies. *J. Mol. Struct.* **2021**, *1223*, 128994. [CrossRef]
33. Devi, J.; Yadav, M.; Jindal, D.K.; Kumar, D.; Poornachandra, Y. Synthesis, spectroscopic characterization, biological screening and in vitro cytotoxic studies of 4-methyl-3-thiosemicarbazone derived Schiff bases and their Co(II), Ni(II), Cu(II) and Zn(II) complexes. *Appl. Organomet. Chem.* **2019**, *33*, 1–23. [CrossRef]
34. Basri, R.; Khalid, M.; Shafiq, Z.; Tahir, M.S.; Khan, M.U.; Tahir, M.N.; Naseer, M.M.; Braga, A.A.C. Exploration of chromone-based thiosemicarbazone derivatives: SC-XRD/DFT, spectral (IR, UV−Vis) characterization, and quantum chemical analysis. *ACS Omega* **2020**, *5*, 30176–30188. [CrossRef] [PubMed]
35. Nakamoto, K. *Infrared and Ramon Spectra of Inorganic and Coordination Compounds*; Wiley Interscience: New York, NY, USA, 1997.
36. Lalović, M.M.; Vojinović-Ješić, L.S.; Jovanović, L.S.; Leovac, V.M.; Češljević, V.I.; Divjaković, V. Synthesis, characterization and crystal structure of square-pyramidal copper(II) complexes with pyridoxylidene aminoguanidine. *Inorganica Chim. Acta* **2012**, *388*, 157–162. [CrossRef]
37. Jelić, M.G.; Boukos, N.; Lalović, M.M.; Romčević, N.Ž.; Leovac, V.M.; Hadžić, B.B.; Baloš, S.S.; Jovanović, L.S.; Slankamenac, M.P.; Živanov, M.B.; et al. Synthesis, structure and photoluminescence properties of copper(II) and cobalt(III) complexes with pyridoxalaminoguanidine. *Opt. Mater.* **2013**, *35*, 2728–2735. [CrossRef]
38. Lalović, M.M.; Jovanović, L.S.; Vojinović-Ješić, L.S.; Leovac, V.M.; Češljević, V.I.; Rodić, M.V.; Divjaković, V. Syntheses, crystal structures, and electrochemical characterizations of two octahedral iron(III) complexes with Schiff base of pyridoxal and aminoguanidine. *J. Coord. Chem.* **2012**, *65*, 4217–4229. [CrossRef]
39. Gak Simić, K.; Đorđević, I.; Lazić, A.; Radovanović, L.; Petković-Benazzouz, M.; Rogan, J.; Trišović, N.; Janjić, G. On the supramolecular outcomes of fluorination of cyclohexane-5-spirohydantoin derivatives. *CrystEngComm* **2021**, *23*, 2606–2622. [CrossRef]
40. Jevtovic, V.; Alshammari, N.; Latif, S.; Alsukaibi, A.K.D.; Humaidi, J.; Alanazi, T.Y.A.; Abdulaziz, F.; Matalka, S.I.; Pantelić, N.Đ.; Marković, M.; et al. Synthesis, Crystal Structure, Theoretical Calculations, Antibacterial Activity, Electrochemical Behavior, and Molecular Docking of Ni(II) and Cu(II) Complexes with Pyridoxal-Semicarbazone. *Molecules* **2022**, *27*, 6322. [CrossRef]
41. Jevtovic, V.; Alshamari, A.K.; Milenković, D.; Dimitrić Marković, J.; Marković, Z.; Dimić, D. The Effect of Metal Ions (Fe, Co, Ni, and Cu) on the Molecular-Structural, Protein Binding, and Cytotoxic Properties of Metal Pyridoxal-Thiosemicarbazone Complexes. *Int. J. Mol. Sci.* **2023**, *24*, 11910. [CrossRef]
42. Jevtovic, V.; Alhar, M.S.O.; Milenković, D.; Marković, Z.; Dimitrić Marković, J.; Dimić, D. Synthesis, Structural Characterization, Cytotoxicity, and Protein/DNA Binding Properties of Pyridoxylidene-Aminoguanidine-Metal (Fe, Co, Zn, Cu) Complexes. *Int. J. Mol. Sci.* **2023**, *24*, 14745. [CrossRef]
43. Serwecińska, L. Antimicrobials and Antibiotic-Resistant Bacteria: A Risk to the Environment and to Public Health. *Water* **2020**, *12*, 3313. [CrossRef]
44. Zhang, Z.; Zhang, Q.; Wang, T.; Xu, N.; Lu, T.; Hong, W.; Penuelas, J.; Gillings, M.; Wang, M.; Gao, W.; et al. Assessment of global health risk of antibiotic resistance genes. *Nat. Commun.* **2022**, *13*, 1553. [CrossRef] [PubMed]
45. Allen, H.K.; Donato, J.; Wang, H.H.; Cloud-Hansen, K.A.; Davies, J.; Handelsman, J. Call of the wild: Antibiotic resistance genes in natural environments. *Nat. Rev. Microbiol.* **2010**, *8*, 251–259. [CrossRef] [PubMed]
46. Turecka, K.; Chylewska, A.; Rychłowski, M.; Zakrzewska, J.; Waleron, K. Antibacterial Activity of Co(III) Complexes with Diamine Chelate Ligands against a Broad Spectrum of Bacteria with a DNA Interaction Mechanism. *Pharmaceutics* **2021**, *13*, 946. [CrossRef]
47. Silhavy, T.J.; Kahne, D.; Walker, S. The Bacterial Cell Envelope. *Cold Spring Harb. Perspect. Biol.* **2010**, *2*, a000414. [CrossRef]
48. Subhan, A.; Tahir, K.; Nazir, S.; Khan, A.U.; Albalawi, K.; Latif, S.; El-Zahhar, A.A.; Munshi, A.M.; Saleh, E.A.M.; Alghamdi, M.M. Synthesis of platinum decorated copper oxide doped layer graphite carbon nitrite: An efficient photocatalyst for disintegration of bacteria and decomposition of dye. *Mater. Today Commun.* **2022**, *33*, 104395. [CrossRef]
49. Arooj, A.; Tahir, K.; Ullah Khan, A.; Khan, A.; Jevtovic, V.; El-Zahhar, A.A.; Alghamdi, M.M.; Al-Shehri, H.S.; Abdu Musad Saleh, E.; Asghar, B.H. One-step fabrication of surfactant mediated Pd/SiO2, A prospect toward therapeutic and photocatalytic applications. *Inorg. Chem. Commun.* **2022**, *142*, 109692. [CrossRef]
50. Nuti, E.; Cuffaro, D.; D'Andrea, F.; Rosalia, L.; Tepshi, L.; Fabbi, M.; Carbotti, G.; Ferrini, S.; Santamaria, S.; Camodeca, C.; et al. Sugar-Based Arylsulfonamide Carboxylates as Selective and Water-Soluble Matrix Metalloproteinase-12 Inhibitors. *ChemMedChem* **2016**, *11*, 1626–1637. [CrossRef]

51. Xu, S.; Uddin, M.J.; Banerjee, S.; Duggan, K.; Musee, J.; Kiefer, J.R.; Ghebreselasie, K.; Rouzer, C.A.; Marnett, L.J. Fluorescent indomethacin-dansyl conjugates utilize the membrane-binding domain of cyclooxygenase-2 to block the opening to the active site. *J. Biol. Chem.* **2019**, *294*, 8690–8698. [CrossRef]
52. Lee, J.; Kim, J.; Koh, J.S.; Chung, H.-H.; Kim, K.-H. Hydantoin derivatives as non-peptidic inhibitors of Ras farnesyl transferase. *Bioorg. Med. Chem. Lett.* **2006**, *16*, 1954–1956. [CrossRef]
53. Kang, S.; Li, H.; Tang, W.; Martásek, P.; Roman, L.J.; Poulos, T.L.; Silverman, R.B. 2-Aminopyridines with a Truncated Side Chain To Improve Human Neuronal Nitric Oxide Synthase Inhibitory Potency and Selectivity. *J. Med. Chem.* **2015**, *58*, 5548–5560. [CrossRef]
54. Alderton, W.K.; Cooper, C.E.; Knowles, R.G. Nitric oxide synthases: Structure, function and inhibition. *Biochem. J.* **2001**, *357*, 593. [CrossRef]
55. Zhou, L.; Zhu, D.-Y. Neuronal nitric oxide synthase: Structure, subcellular localization, regulation, and clinical implications. *Nitric Oxide* **2009**, *20*, 223–230. [CrossRef] [PubMed]
56. CrysAlisPRO. *Oxford Diffraction*; Agilent Technologies UK Ltd.: Yarnton, UK, 2017.
57. Turner, M.J.; McKinnon, J.J.; Wolff, S.K.; Grimwood, D.J.; Spackman, P.R.; Jayatilaka, D.; Spackman, M.A. CrystalExplorer17 2017.
58. Spackman, M.A.; Jayatilaka, D. Hirshfeld surface analysis. *CrystEngComm* **2009**, *11*, 19–32. [CrossRef]
59. Grabowsky, S.; Dean, P.M.; Skelton, B.W.; Sobolev, A.N.; Spackman, M.A.; White, A.H. Crystal packing in the 2-R,4-oxo-[1,3-a/b]-naphthodioxanes – Hirshfeld surface analysis and melting point correlation. *CrystEngComm* **2012**, *14*, 1083–1093. [CrossRef]
60. Frisch, M.J.; Trucks, G.W.; Schlegel, H.B.; Scuseria, G.E.; Robb, M.A.; Cheeseman, J.R.; Scalmani, G.; Barone, V.; Mennucci, B.; Petersson, G.A.; et al. *Gaussian 09, Revision C.01*; Gaussian, Inc.: Wallingford, CT, USA, 2009.
61. Becke, A.D. Density-functional exchange-energy approximation with correct asymptotic behavior. *Phys. Rev. A* **1988**, *38*, 3098–3100. [CrossRef]
62. Dunning, T.H. Gaussian basis sets for use in correlated molecular calculations. I. The atoms boron through neon and hydrogen. *J. Chem. Phys.* **1989**, *90*, 1007. [CrossRef]
63. Hay, P.J.; Wadt, W.R. Ab initio effective core potentials for molecular calculations. Potentials for K to Au including the outermost core orbitale. *J. Chem. Phys.* **1985**, *82*, 299–310. [CrossRef]
64. Hay, P.J.; Wadt, W.R. Ab initio effective core potentials for molecular calculations. Potentials for the transition metal atoms Sc to Hg. *J. Chem. Phys.* **1985**, *82*, 270–283. [CrossRef]
65. Khan, A.U.; Nazir, S.; El-Keblawy, A.; Tahir, K.; Abdel-Hafez, S.H.; AL-Abdulkarim, H.A.; Jevtovic, V.; Ibrahim, M.M.; Al-Shehri, H.S.; Hegab, K.H. Uncaria rhynchophylla mediated Ag/NiO nanocomposites: A new insight for the evaluation of cytotoxicity, antibacterial and photocatalytic applications. *Photodiagnosis Photodyn. Ther.* **2022**, *37*, 102681. [CrossRef]
66. Khan, A.U.; Khan, Q.U.; Tahir, K.; Ullah, S.; Arooj, A.; Li, B.; Rehman, K.U.; Nazir, S.; Khan, M.U.; Ullah, I. A Tagetes minuta based eco-benign synthesis of multifunctional Au/MgO nanocomposite with enhanced photocatalytic, antibacterial and DPPH scavenging activities. *Mater. Sci. Eng. C* **2021**, *126*, 112146. [CrossRef]
67. Batool, I.; Albalawi, K.; Khan, A.U.; Tahir, K.; Haq Khan, Z.U.; Zaki, M.E.A.; Musad Saleh, E.A.; Alabbad, E.A.; Althagafi, T.M.; Abdulaziz, F. The construction of novel CuO/SnO2@g-C3N4 photocatalyst for efficient degradation of ciprofloxacin, methylene blue and photoinhibition of bacteria through efficient production of reactive oxygen species. *Environ. Res.* **2023**, *231*, 116086. [CrossRef]
68. Dilawar, S.; Albalawi, K.; Khan, A.U.; Tahir, K.; Zaki, M.E.A.; Musad Saleh, E.A.; Almarhoon, Z.M.; Althagafi, T.M.; El-Zahhar, A.A.; El-Bialy, E. Rapid photodegradation of toxic organic compounds and photo inhibition of bacteria in the presence of novel hydrothermally synthesized Ag/Mn–ZnO nanomaterial. *Environ. Res.* **2023**, *231*, 116093. [CrossRef]
69. Khan, M.J.; Tahir, K.; El-Zahhar, A.A.; Arooj, A.; AL-Abdulkarim, H.A.; Saleh, E.A.M.; Nazir, S.; Al-Shehri, H.S.; Husain, K.; Khan, A.U. Facile synthesis of silver modified zinc oxide nanocomposite: An efficient visible light active nanomaterial for bacterial inhibition and dye degradation. *Photodiagnosis Photodyn. Ther.* **2021**, *36*, 102619. [CrossRef]
70. Khan, M.A.; Khan, A.U.; Tahir, K.; Othman Alhar, M.S.; Zaki, M.E.A.; Althagafi, T.M.; Alanazi, A.A.; Al-Saeedi, S.I.; Al-Shehri, H.S.; Nazir, S. Synthesis of Zr–Fe_2O_3/In_2O_3 photocatalyst by novel hydrothermal method for highly selective photo inhibition of pathogens, pollutant degradation and DPPH stabilization. *Mater. Chem. Phys.* **2023**, *302*, 127746. [CrossRef]
71. Saleh, E.A.M.; Khan, A.U.; Tahir, K.; Almehmadi, S.J.; AL-Abdulkarim, H.A.; Alqarni, S.; Muhammad, N.; AL Dawsari, A.M.; Nazir, S.; Ullah, A. Phytoassisted synthesis and characterization of palladium nanoparticles (PdNPs); with enhanced antibacterial, antioxidant and hemolytic activities. *Photodiagnosis Photodyn. Ther.* **2021**, *36*. [CrossRef] [PubMed]
72. Ullah, I.; Tahir, K.; Khan, A.U.; Albalawi, K.; Li, B.; El-Zahhar, A.A.; Jevtovic, V.; Al-Shehri, H.S.; Asghar, B.H.; Alghamdi, M.M. Facile fabrication of Ag nanoparticles: An advanced material for antioxidant, infectious therapy and photocatalytic applications. *Inorg. Chem. Commun.* **2022**, *141*, 109539. [CrossRef]
73. Gfeller, D.; Grosdidier, A.; Wirth, M.; Daina, A.; Michielin, O.; Zoete, V. SwissTargetPrediction: A web server for target prediction of bioactive small molecules. *Nucleic Acids Res.* **2014**, *42*, W32–W38. [CrossRef]
74. Biasini, M.; Bienert, S.; Waterhouse, A.; Arnold, K.; Studer, G.; Schmidt, T.; Kiefer, F.; Cassarino, T.G.; Bertoni, M.; Bordoli, L.; et al. SWISS-MODEL: Modelling protein tertiary and quaternary structure using evolutionary information. *Nucleic Acids Res.* **2014**, *42*, 252–258. [CrossRef] [PubMed]
75. Trott, O.; Olson, A.J. AutoDock Vina: Improving the speed and accuracy of docking with a new scoring function, efficient optimization, and multithreading. *J. Comput. Chem.* **2009**, *31*, 455–461. [CrossRef] [PubMed]

76. Morris, G.M.; Huey, R.; Lindstrom, W.; Sanner, M.F.; Belew, R.K.; Goodsell, D.S.; Olson, A.J. AutoDock4 and AutoDockTools4: Automated docking with selective receptor flexibility. *J. Comput. Chem.* **2009**, *30*, 2785–2791. [CrossRef] [PubMed]
77. BIOVIA. *Dassault Systèmes, Discovery Studio 2016*; Dassault Systèmes: San Diego, CA, USA, 2016; Dassault Systèmes BIOVIA, Discovery Studio Modeling Environment (Release 2017) 2016.